High-order methods for thermal behavior of plate structures with internal heat sources

High-order methods for thermal behaviour of plate structures with internal heat sources

Rachid Bouna[1], Nouh Izem[1], Mohammed Seaid[2], M Shadi Mohamed[3,*]

[1] *Laboratory of Engineering Sciences, Faculty of Science, Ibn Zohr University Agadir, Morocco.*
[2] *School of Engineering and Computing Sciences, University of Durham, UK.*
[3] *School of Energy, Geoscience, Infrastructure and Society, Heriot-Watt University, Edinburgh EH14 4AS, UK.*

Abstract

The paper proposes solving transient heat transfer in plates using high-order isogeometric analysis and high-order time integration schemes. The problem is often faced in fire-structure interaction where the heat transfer is coupled with the stress analysis. A major advantage for the proposed approach comes from high order continuity between elements. Thus, the need for rotational degrees of freedom is eliminated when analyzing the stresses in plates and the same mesh can also be used to recover the heat transfer patterns. To achieve the full potential of such high-order finite elements in space, we also use high-order time integration schemes so that the numerical solution can be significantly more accurate than the standard approaches. Furthermore, the isogeometric analysis is also used to represent the exact geometry thanks to the basis functions generated from Non-Uniform Rational B-Splines. Several test examples for the transient diffusion problem are presented. Compared to standard methods and for a prescribed accuracy the proposed approach requires significantly fewer degrees of freedom and a corresponding improvement in the computational efficiency.

Keywords: Heat conduction, Heat transfer, Isogeometric analysis, Finite element methods, High-order methods, Implicit time integration, NURBS

1 Introduction

To simulate fire-structure interaction the finite element method (FEM) is often used to assess the temperature and the displacement fields within structural elements. In this work we focus on thin-walled structures such as slabs, panels or general shells. Such elements are often treated as two-dimensional structures because their thickness is orders of magnitude smaller than the other dimensions. The approximation into two-dimensional structures significantly reduces the degrees of freedom needed to accurately solve the problem compared to the three-dimensional case where highly refined mesh grids are needed to maintain a reasonable elements aspect ratio. More precisely, we focus on planar elements so that the fire-structure interaction can be well approximated by considering the heat source to be within the structural plane. The fire-structure interaction is usually assessed on three levels in a computational procedure: (i) the fire simulation is achieved using the well-established techniques from computational fluid dynamics, (ii) in the next level the fire is introduced as a heat source applied inside the domain and/or on its boundaries, and (iii) finally, the thermo-mechanical behaviour of the elements is evaluated using a numerical approach such as the FEM, see for example [9, 21] and further references are therein. In the current work, we look into

*Corresponding author: m.s.mohamed@hw.ac.uk

the last level where the fire is introduced as a single or multiple heat sources. Particularly, we focus in this study on the heat conduction within a plate. For modelling the thermal dynamics of the problem the heat diffusion equation can be used. To recover the heat field we use the Isogeometric Analysis (IGA) [11], where the same Non-Uniform Rational B-Splines (NURBS) used to model the geometry in a CAD system are also used to evaluate the heat field. The approach enables modelling the exact geometry with coarse elements. Hence, unnecessary mesh refinement to capture the exact geometry can be avoided. Furthermore, using the NURBS high-order continuity in the solution is easily achievable compared to only C^0 continuity offered by the standard Lagrangian finite elements [11, 3]. The high-order continuity eliminates the need for rotational degrees of freedom otherwise necessary for structural elements such as plates and shells [17, 29], hence, leading to a major reduction in the number of degrees of freedom needed to solve a problem [17]. Furthermore, the Gibbs phenomena observed at higher order Lagrangian finite elements is also reduced using IGA [18, 8]. Therefore, one may also benefit from using higher orders NURBS which we focus on in this paper.

It should be stressed that the IGA approach for elliptical diffusion type problems was initially presented in [31]. A similar approach is developed within the boundary element framework [1] while an adaptive isogeometric analysis is presented in [35]. The IGA has later been employed for several heat transfer problems in both physical and engineering applications. For example, the work published in [2] investigated the IGA for evaluating the effect of thermal diffusion on a microstructure of a blend of polymers. The method coupled with a control volume approach has been applied to analyze the heat transfer in non-uniformly heated plates in [16]. The IGA has also been implemented to analyze the heat transfer in an axial-flux permanent magnet in [33]. Furthermore, the potential to integrate the IGA within a commercial framework is explored in [15]. Compared to previous works where only steady-state problems are considered, in this paper we aim to investigate the performance of the IGA for transient problems so that the full time history of the problem is considered. In the present study we develop an IGA approach that is capable of accurately approximating numerical solutions of the time-dependent heat conduction problem. The aim is to combine high-order discretizations in time and space. To deal with the transient nature of the heat conduction, the FEM is usually combined with a time integration technique. The use of a high-order spatial discretization makes it necessary to also apply a high-order time integration scheme to achieve a consistent convergence rate in space and time [32]. For solving first-order transient systems such as the one presented in this work, the backward Euler is a popular method but it is only a first-order scheme and hence, over-dissipative. Another popular second-order method is the Crank-Niclson which often leads to unconditional stability. However, it still suffers from non-physical oscillations when the mesh grid is fine and/or the timestep is large [19]. The second-order backward differentiation formula can suppress the non-physical oscillations but to initiate the procedure it requires other single step methods such as Runge-Kutta schemes. The implicit Runge-Kutta family of time stepping methods can achieve high-order accuracy but they requires solving a large system of algebraic equations. Thus, the computational costs are increased in order to achieve the accuracy as well as the unconditional stability [4]. Recently, the generalised single-step method is developed and implemented in several applications, see [6, 19, 20, 34] among others. An extensive review of time integration algorithms for different transient systems can be found in [32].

Although it is almost a decade since IGA has been introduced for solving heat conduction equations but in general only low-order time stepping methods are studied. In this paper, we aim to cover this gap in the literature by studying high-order IGA approximations combined with high-order time integrations. The coupling is important to study as a high-order spatial discretization requires a high-order time integration scheme to achieve convergence rates that are consistent in space and time [32]. Moreover, we also discuss the IGA in the context of transient diffusion problems where previously only steady-state problems were discussed. Although the presented work focuses on heat conduction within the thermo-mechanical context but the work here is also very relevant to other applications including for example the growth-phenomena [28, 13] and electro-mechanics [24, 12] where the diffusion also needs to be solved. Major motivation for this analysis is its application in a future work to forecast thermal stresses in plates due to heat conduction. A significant amount of the work is dedicated to developing a massively parallel solver to

implement the proposed numerical algorithms. Results are presented for several problems of transient heat transfer problems including a diffusion problem with known analytical solution and heat conduction with multiple sources. The results demonstrate good resolution of the considered implicit time integration schemes with high-order accuracy in approximating the solution in time and space. The problems considered here are also representative examples for many practical time-dependent heat transfer applications. Further, the results obtained using the IGA studied in the current work are also compared to those obtained using the conventional FEM.

The rest of this paper is organized as follows. In section 2 we discretize the transient heat conduction using multiple time-integration schemes. This section includes also the resulting finite element weak formulations of the problem under study. The isogeometric approximations used for solving the heat conduction is presented in section 3. The NURBS-based procedure and the assembly of the IGA matrices are also presented there. Numerical results are then shown in section 4 including several examples of unsteady diffusion equations and a heat conduction problem with multiple heat sources as well as comparisons with three-dimensional results. We examine the numerical performance of the proposed time integration schemes for the selected problems. Final concluding remarks are summarized in section 5.

2 Time integration schemes

We aim to solve the linear heat equation inside the domain of interest $\Omega \subset \mathbb{R}^2$ and a boundary Γ within the time interval $[0, T]$,

$$\frac{\partial u}{\partial t} - \lambda \nabla^2 u = f, \qquad (t, \mathbf{x}) \in]0, T] \times \Omega. \tag{1}$$

Here λ is the heat diffusion coefficient, t time, $\mathbf{x} = (x, y)^\top$ the Cartesian coordinates and ∇ is the nabla operator. Note that any heat sources or sinks inside the domain are introduced using the source term $f(t, \mathbf{x})$. The ambient temperature is represented in the problem using a mixed-type boundary condition applied on Γ as

$$\alpha u + \frac{\partial u}{\partial \mathbf{n}} = g, \quad (t, \mathbf{x}) \in]0, T] \times \Gamma, \tag{2}$$

where α is a non-zero constant and $\mathbf{n}$ is the outward-pointing normal vector on Γ. The ambient temperature or any heat sources can be introduced using the boundary function $g(t, \mathbf{x})$. The initial condition is defined using

$$u = u_0, \quad \text{at} \quad t = 0 \quad \text{and} \quad \mathbf{x} \in \Omega, \tag{3}$$

where $u_0(0, \mathbf{x})$ is known. To solve the unsteady boundary-value problem (1)-(3) we first discretize the time span $[0, T]$ into N_t uniform timesteps $[t_n, t_{n+1}]$ and then the domain Ω into a set of element. The timestep size is given by $\Delta t = t_{n+1} - t_n$. A semi-discrete formulation of (1) is given as

$$\frac{u_n - u_{n+1}}{\Delta t} - \lambda(\theta - 1)\nabla^2(u_{n+1}) + \lambda\theta\nabla^2(u_n) = (\theta - 1)f_{n+1} - \theta f_n, \tag{4}$$

with a θ-time stepping scheme being used. The choice of θ then defines the time integration method. Here, the notation w_n refers to a generic function w at a time instant t_n. Next, we discuss the time integration schemes considered in the current study.

2.1 First-order backward Euler scheme

Taking $\theta = 0$ in (4), it leads to the first-order Backward Euler time integration method. The resulting system to be solved is then given as

$$-\Delta t\lambda\nabla^2 u_{n+1} + u_{n+1} = u_n + \Delta t f_{n+1}. \tag{5}$$

To solve equation (5) we build a standard isogeometric analysis formulation. First we multiply the equation with a test function v and then integrate over Ω to obtain

$$-\int_{\Omega} \Delta t\lambda v\nabla^2 u_{n+1}\, d\Omega + \int_{\Omega} v u_{n+1}\, d\Omega = \int_{\Omega} v(u_n + \Delta t f_{n+1})\, d\Omega.$$

Applying the divergence theorem

$$-\int_{\Gamma} \Delta t\lambda v\nabla u_{n+1}\cdot \mathbf{n}\, d\Gamma + \int_{\Omega} (\Delta t\lambda \nabla v\cdot\nabla u_{n+1} + v u_{n+1})\, d\Omega = \int_{\Omega} v(u_n + \Delta t f_{n+1})\, d\Omega. \tag{6}$$

Substituting the boundary condition (2) into equation (6) we obtain the weak form: Find u in the Sobolev space $H^1(\Omega)$ such as

$$\Delta t\lambda \oint_{\Gamma} \Big(\alpha u_{n+1} - g_{n+1}\Big) v\, d\Gamma + \Delta t\lambda \int_{\Omega} \nabla v\cdot\nabla u_{n+1}\, d\Omega + \int_{\Omega} v u_{n+1}\, d\Omega = \int_{\Omega} v u_n\, d\Omega + \Delta t \int_{\Omega} v f_{n+1}\, d\Omega. \tag{7}$$

The above statement is valid for any test function $v \in H^1(\Omega)$. In this work we focus on test functions constructed using the NURBS. To find the solution u_{n+1}, the weak formulation (7) needs to be solved at every timestep. Furthermore, Δt choice is only dependent on the accuracy of the computed solutions thanks to the unconditional stability of the Backward Euler for linear problems.

2.2 Second-order Adams-Bashforth scheme

To improve the solution accuracy without refining the timestep one may also increase the integration order. In this section we introduce the second-order implicit Adams-Bashforth method [26]. The semi-discrete formulation is now given by

$$-\lambda\nabla^2 u_{n+1} + \frac{u_{n-1} - 4u_n + 3u_{n+1}}{2\Delta t} = f_{n+1},$$

Again we follow the same steps as before to obtain the following weak formulation: Find u in the Sobolev space $H^1(\Omega)$ such that

$$-2\lambda\Delta t \int_{\Omega} v\nabla^2 u_{n+1}\, d\Omega + 3\int_{\Omega} v u_{n+1}\, d\Omega = \int_{\Omega} v(2\Delta t f_{n+1} + 4u_n - u_{n-1})\, d\Omega, \qquad \forall v \in H^1(\Omega).$$

Using the divergence theorem and then replacing the boundary condition, the above equation becomes

$$\begin{aligned} 2\lambda\Delta t \int_{\Omega} \nabla v\cdot\nabla u_{n+1}\, d\Omega + 3\int_{\Omega} v u_{n+1}\, d\Omega + 2\lambda\Delta t \oint_{\Gamma} \Big(\alpha u_{n+1} - g_{n+1}\Big) v\, d\Gamma = \\ 2\Delta t \int_{\Omega} v f_{n+1}\, d\Omega + 4\int_{\Omega} v u_n\, d\Omega - \int_{\Omega} v u_{n-1}\, d\Omega, \end{aligned} \tag{8}$$

which is again valid for any test function $v \in H^1(\Omega)$. Here we note that only one initial condition is given at time $t = 0$. The second condition is obtained using the backward Euler method.

2.3 Third-order Adams-Bashforth method

Next, we also formulate a weak formulation for the third-order implicit Adams-Bashforth method [26] and the diffusion problem can be rewritten as

$$\frac{11u_{n+1} - 18u_n + 9u_{n-1} - 2u_{n-2}}{6\Delta t} - \lambda\nabla^2 u_{n+1} = f_{n+1},$$

or simply

$$11u_{n+1} - 18u^n + 9u_{n-1} - 2u_{n-2} - 6\lambda\Delta t\nabla^2 u_{n+1} = 6\Delta t f_{n+1}.$$

Again, we multiply by the test function v and then integrate over Ω to get the weak form: Find u in the Sobolev space $H^1(\Omega)$ such that

$$\begin{aligned} 11\int_\Omega v u_{n+1}\,d\Omega - 6\lambda\Delta t\int_\Omega v\nabla^2 u_{n+1}\,d\Omega = \\ \int_\Omega v(6\Delta t f_{n+1} + 18u_n - 9u_{n-1} + 2u_{n-2})\,d\Omega, \qquad \forall v \in H^1(\Omega). \end{aligned} \tag{9}$$

Using the divergence theorem and finally substituting the boundary conditions we obtain

$$\begin{aligned} 6\lambda\Delta t\int_\Omega \nabla v\cdot\nabla u_{n+1}\,d\Omega + 11\int_\Omega v u_{n+1}\,d\Omega + 6\lambda\Delta t\oint_\Gamma \Big(\alpha u_{n+1} - g_{n+1}\Big)v\,d\Gamma = \\ 6\Delta t\int_\Omega v f_{n+1}\,d\Omega + 18\int_\Omega v u_n\,d\Omega - 9\int_\Omega v u_{n-1} + 2\int_\Omega v u_{n-2}\,d\Omega, \end{aligned} \tag{10}$$

which is valid $\forall v \in H^1(\Omega)$. It should be pointed out that the time stepping (10) requires the current solution u_n, the past solutions u_{n-1} and u_{n-2} to evaluate u_{n+1} which is the following timestep. At initial time $n = 0$, u_n is given and the first-order backward Euler scheme is used for the first step to update the solution u_{n-1} whereas, the solution u_{n-2} is obtained using the second-order Adams-Bashforth method.

3 Isogeometric analysis of transient heat conduction

In this section we discuss the construction of the Isogeometric basis functions to be used here as test functions in the weak formulations described above. Since the IGA basis functions are built with Non-Uniform Rational B-splines (NURBS) we first discuss NURBS. It should be noted that for the purpose of comparison we also consider the standard Lagrangian finite element basis functions. However, for sake of brevity we only describe the IGA basis functions here. The interested reader are referred to [14, 36, 11, 23, 5, 30, 31] where more details can be found.

3.1 NURBS basis functions

The NURBS are defined on a knot vector which represents the coordinates in a parametric space as a set of non-decreasing real numbers, *i.e.*

$$\Xi = \{\xi_0, \xi_1, \ldots, \xi_{n+p}\},$$

where n is the number of basis functions and p the spline order. Here, we should note that the index in ξ_i refers to the location in the knot vector and not the timestep. All the basis functions discussed in this work are independent on time. We can then define a B-spline basis function for $p = 0$ as the following piecewise constants

$$N_{i,0} = \begin{cases} 1, & \text{if} \quad \xi_i \le \xi < \xi_{i+1}, \\ \\ 0, & \text{elsewhere.} \end{cases}$$

For $p \ge 1$ the B-splines are defined recursively by

$$N_{i,p} = \frac{\xi - \xi_i}{\xi_{i+p} - \xi_i} N_{i,p-1} + \frac{\xi_{+p+1} - \xi}{\xi_{i+p+1} - \xi_{i+1}} N_{i+1,p-1}, \tag{11}$$

where we note that the fraction of the form $\frac{0}{0}$ is considered to be zero. More details on this consideration can be found in [25]. Thus we may define the Non-Uniform Rational B-splines as

$$R_i^p = \frac{N_{i,p} w_i}{\sum_{\hat{\imath}=1}^{n} N_{\hat{\imath},p} w_{\hat{\imath}}}, \tag{12}$$

with the weight w_i being associated with the i-th B-spline function. In the two-dimensional problems, the NURBS functions are defined as the tensor product between their two one-dimensional counterparts as

$$R_{i,j}^{p,q} = \frac{N_{i,p} M_{j,q} w_{i,j}}{\sum_{\hat{j}=1}^{m} \sum_{\hat{i}=1}^{n} N_{\hat{i},p} M_{\hat{j},q} w_{\hat{i},\hat{j}}}. \tag{13}$$

Here, a second set of B-splines of degree q, namely, $M_{j,q}(\eta)$ is defined on a second knot vector $\Xi_2 = \{\eta_1, \eta_2, \ldots, \eta_{m+q+1}\}$ with m being the number of the basis functions of $M_{j,q}(\eta)$. As shown in Figure 1, the mapping between the parametric space $\widehat{\Omega} = [\xi_0, \xi_{n+p}] \times [\eta_0, \eta_{m+q}]$ and the physical space Ω is given by

$$\mathbf{F} = \sum_{j=1}^{m} \sum_{i=1}^{n} R_{i,j}^{p,q} \mathbf{C}_{i,j} = [x, y]^{\top}, \tag{14}$$

with $\mathbf{C}_{i,j}$ being the physical space control points. In what follows, the notation $R_{i,j}(\xi, \eta) = R_{i,j}^{p,q}(\xi, \eta)$ is used. We also restrict ourselves to the case where $q = p$ and $m = n$ for simplicity in the presentation. The geometry function $\mathbf{F}(\xi, \eta)$ can be defined for a single patch via

$$\mathbf{F} = \sum_{j=1}^{m} \sum_{i=1}^{n} R_{ij} \mathbf{C}_{ij}, \tag{15}$$

with the bivariate NURBS $R_{ij}(\xi, \eta)$ on the patch $\Omega_0 = [0, 1]^2$ and the control points $\mathbf{C}_{ij} \in \mathbb{R}^2$. In the isogeometric analysis, $R_{ij}(\xi, \eta)$ are also used as test functions. Employing the so-called "push forward" operator from Ω_0 onto Ω, we get for the Dirichlet-type boundary conditions

$$\mathbf{V}_h = \Big\{ \varphi_k \mid \quad \varphi_k = g \quad \text{on } \partial\Omega, \quad k = 1, 2, 3, \ldots, N_h \Big\} \subset \text{span} \Big\{ R_{ij} \circ \mathbf{F}^{-1} \Big\}_{1 \le i \le n, 1 \le j \le m},$$

and for the Robin-type boundary conditions we get

$$\mathbf{V}_h = \Big\{ \varphi_k \mid \quad k = 1, 2, 3, \ldots, N_h \Big\} \subset \text{span} \Big\{ R_{ij} \circ \mathbf{F}^{-1} \Big\}_{1 \le i \le n, 1 \le j \le m},$$

with $N_h = dim(V_h) = n \times m$. A numerical solution u^h is approximated as

$$u^h = \sum_{i=1}^{n} \sum_{j=1}^{m} R_{ij} \left(\mathbf{F}^{-1} \right) \phi_{ij}. \tag{16}$$

Clearly for Dirichlet-type conditions, some of the coefficients ϕ_{ij} are determined from the boundary condition. Using a lexicographical numbering such that the unknown coefficients are written in a vector as

$$\phi = (\phi_{1,1}, \ldots, \phi_{n,1}, \ldots, \phi_{1,m}, \ldots, \phi_{n,m}).$$

The same numbering is used for the assembly of the stiffness matrix, the mass matrix and the right-hand side vector in the semi-discrete systems obtained from IGA. It should be noted that the basis functions of IGA are smoother than those of conventional FEM. Hence, curved boundaries of the computational domain are exactly modelled unlike in the standard FEM. However, the IGA implementation is more involved and the extensions of well-established FEM techniques such as the adaptivity, are not trivial.

3.2 Transformation to the parametric domain

The integration of the functions over the physical domain Ω can be transformed into integrals over the parametric domain Ω_0 (see Figure 1) by means of the geometry function $\mathbf{F}$ and the Jacobian transformation

$$\int_{\Omega} f(x, y)\, dxdy = \int_{\Omega_0} f(\mathbf{F}(\xi, \eta)) \Big| \det \mathbf{DF}(\xi, \eta) \Big|\, d\xi d\eta, \tag{17}$$

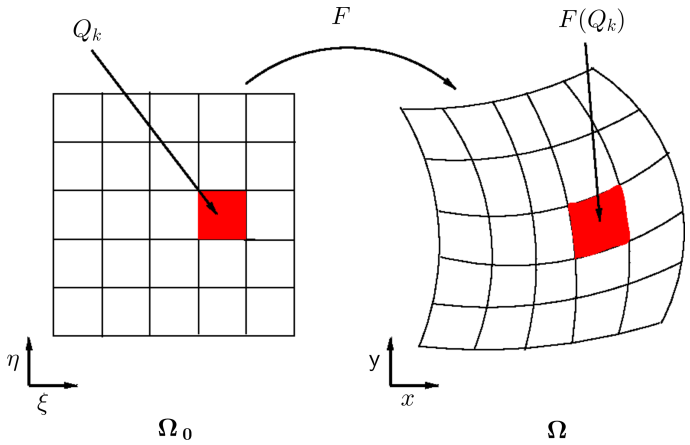

Figure 1: Illustration of the mapping between the parametric and the physical domains.

where $\mathbf{DF}(\xi, \eta)$ is the Jacobian matrix in two-dimensions

$$\mathbf{DF} = \begin{pmatrix} \dfrac{\partial F_1}{\partial \xi} & \dfrac{\partial F_1}{\partial \eta} \\ \dfrac{\partial F_2}{\partial \xi} & \dfrac{\partial F_2}{\partial \eta} \end{pmatrix}.$$

The chain rule is applied to $u(x, y)$ in order to differentiate $u(F(\xi, \eta))$. Thus,

$$\nabla_{(x,y)} u(x, y) = \mathbf{DF}(\xi, \eta)^{-\top} \cdot \nabla_{(\xi,\eta)} u(\xi, \eta). \tag{18}$$

Hence, using the above transformation, the integrals in the weak form become

$$\int_\Omega \nabla u \cdot \nabla v \; dxdy = \int_{\Omega_0} \left(\mathbf{DF}^{-\top} \nabla u\right) \cdot \left(\mathbf{DF}^{-\top} \nabla v\right) |\det \mathbf{DF}| \; d\xi d\eta, \tag{19}$$

$$\int_\Omega uv \; dxdy = \int_{\Omega_0} (u\mathbf{F})(v\mathbf{F}) |\det \mathbf{DF}| \; d\xi d\eta, \tag{20}$$

and

$$\int_\Omega fv \; dxdy = \int_{\Omega_0} (fv)(\mathbf{F}) |\det \mathbf{DF}| \; d\xi d\eta. \tag{21}$$

The previous three integrals can then be performed on elements in the physical domain as

$$\begin{aligned} \int_\Omega \nabla u \cdot \nabla v \; dxdy &= \sum_k \int_{Q_k} \left(\mathbf{DF}^{-\top} \nabla u\right) \cdot \left(\mathbf{DF}^{-\top} \nabla v\right) |\det \mathbf{DF}| \; d\xi d\eta, \\ &= \sum_k \int_{\eta_1^k}^{\eta_2^k} \int_{\xi_1^k}^{\xi_2^k} \left(\mathbf{DF}^{-\top} \nabla u\right) \cdot \left(\mathbf{DF}^{-\top} \nabla v\right) |\det \mathbf{DF}| \; d\xi d\eta, \end{aligned}$$

$$\begin{aligned} \int_\Omega uv \; dxdy &= \sum_k \int_{Q_k} (u\mathbf{F})(v\mathbf{F}) |\det \mathbf{DF}| \; d\xi d\eta, \\ &= \sum_k \int_{\eta_1^k}^{\eta_2^k} \int_{\xi_1^k}^{\xi_2^k} (u\mathbf{F})(v\mathbf{F}) |\det \mathbf{DF}| \; d\xi d\eta, \end{aligned}$$

and

$$\begin{aligned}\int_\Omega fv\; dxdy &= \sum_k \int_{Q_k} (fv)(\mathbf{F})|\det \mathbf{DF}|\; d\xi d\eta, \\ &= \sum_k \int_{\eta_1^k}^{\eta_2^k} \int_{\xi_1^k}^{\xi_2^k} (fv)(\mathbf{F})|\det \mathbf{DF}|\; d\xi d\eta,\end{aligned}$$

where in the parametric domain $Q_k = [\xi_1^k, \xi_2^k] \times [\eta_1^k, \eta_2^k]$ is a quadrilateral. We also stress that the computational domain formed by the sum of all the elements matches exactly the physical domain Ω thanks to the exact geometry representation achieved with NURBS.
The approximation of the weak forms (7), (8) and (10) yield a system of linear equations as in the following

$$[\boldsymbol{A}] \left\{\boldsymbol{u}^{n+1}\right\} = \{\boldsymbol{b}\}. \tag{22}$$

Here, $[\boldsymbol{A}]$ is a symmetric matrix of the size DoF $\times$ DoF, $\{\boldsymbol{b}\}$ is a column vector of the size DoF and $\left\{\boldsymbol{u}^{n+1}\right\}$ is the unknowns column vector of the size DoF where DoF is the number of degrees of freedom. Note that structures of the matrix $[\boldsymbol{A}]$ and the right-hand side vector $\{\boldsymbol{b}\}$ dependent on the considered time integration scheme. For the first-order backward Euler method,

$$[\boldsymbol{A}] = [\boldsymbol{M}] + \Delta t\, [\boldsymbol{K}], \qquad \{\boldsymbol{b}\} = \Delta t \left\{\boldsymbol{f}^{n+1}\right\} + [\boldsymbol{M}] \{\boldsymbol{u}^n\}, \tag{23}$$

with $[\boldsymbol{M}]$ and $[\boldsymbol{K}]$ are respectively, the mass and stiffness matrices generated from the IGA discretization. For the second-order Adams-Bashforth method,

$$[\boldsymbol{A}] = 3\,[\boldsymbol{M}] + 2\Delta t\, [\boldsymbol{K}], \qquad \{\boldsymbol{b}\} = 2\Delta t \left\{\boldsymbol{f}^{n+1}\right\} + 4\,[\boldsymbol{M}] \left\{\boldsymbol{u}^{n-1}\right\} - [\boldsymbol{M}] \{\boldsymbol{u}^n\}, \tag{24}$$

and for the third-order Adams-Bashforth method,

$$[\boldsymbol{A}] = 11\,[\boldsymbol{M}] + 6\Delta t\, [\boldsymbol{K}], \qquad \{\boldsymbol{b}\} = 6\Delta t \left\{\boldsymbol{f}^{n+1}\right\} + 18\,[\boldsymbol{M}] \{\boldsymbol{u}^n\} - 9\,[\boldsymbol{M}] \left\{\boldsymbol{u}^{n-1}\right\} + 2\,[\boldsymbol{M}] \left\{\boldsymbol{u}^{n-2}\right\}. \tag{25}$$

Here, $\left\{\boldsymbol{u}^{n-2}\right\}$, $\left\{\boldsymbol{u}^{n-1}\right\}$ and $\{\boldsymbol{u}^n\}$ are column vectors containing the known solutions u^{n-2}, u^{n-1}, and u^n, respectively. In the present study, to solve the linear system (22) we adopt the multifrontal direct solver presented in [7]. We also note that it is enough to invert the system matrix at the first time step and reused inversion at later time steps after updating the right-hand side.

4 Numerical examples

Now we evaluate the proposed approach for heat transfer in plates where different spatial and temporal approximation orders are compared. In all the presented results, the computational domain is discretized using quadrilateral elements by a single patch parametrization. The material properties are assumed to be time independent. The numerical integrations are evaluated using the Gauss quadrature where the number of integration points equals the polynomial order plus one *i.e.* $(p+1)$ in each parametric direction and a total of $(p+1) \times (p+1)$ integration points per plate element. Here, we note that using a higher number of integration points does not improve the accuracy in the presented results. In the presented results the first test problem is deliberately chosen to have an analytical solution so that the error in the numerical solution can be measured. However, in the remaining test cases no analytical solutions are available and it is only possible to solve these problems with numerical methods.
If the analytical solution is available the L^2-error at time t_n can be evaluated using

$$L^2\text{-error} = \sqrt{\int_\Omega |u_h^n - u_{\text{exact}}^n|^2\; d\Omega},$$

where u_h^n and u_{exact}^n denote respectively, the numerical and the exact solutions at the gridpoint $\mathbf{x}_h$ and time t_n. In the sequel we use the terminology IGA-Euler, IGA-BDF2 and IGA-BDF3 for referring to the coupled IGA with the first-order backward Euler scheme, IGA with the second-order Adams-Bashforth scheme, and IGA with the third-order Adams-Bashforth scheme, respectively. To complete the computations an Intel® Core(TM) i7-7500U @ 2.70GHz with 16 GB of RAM are used.

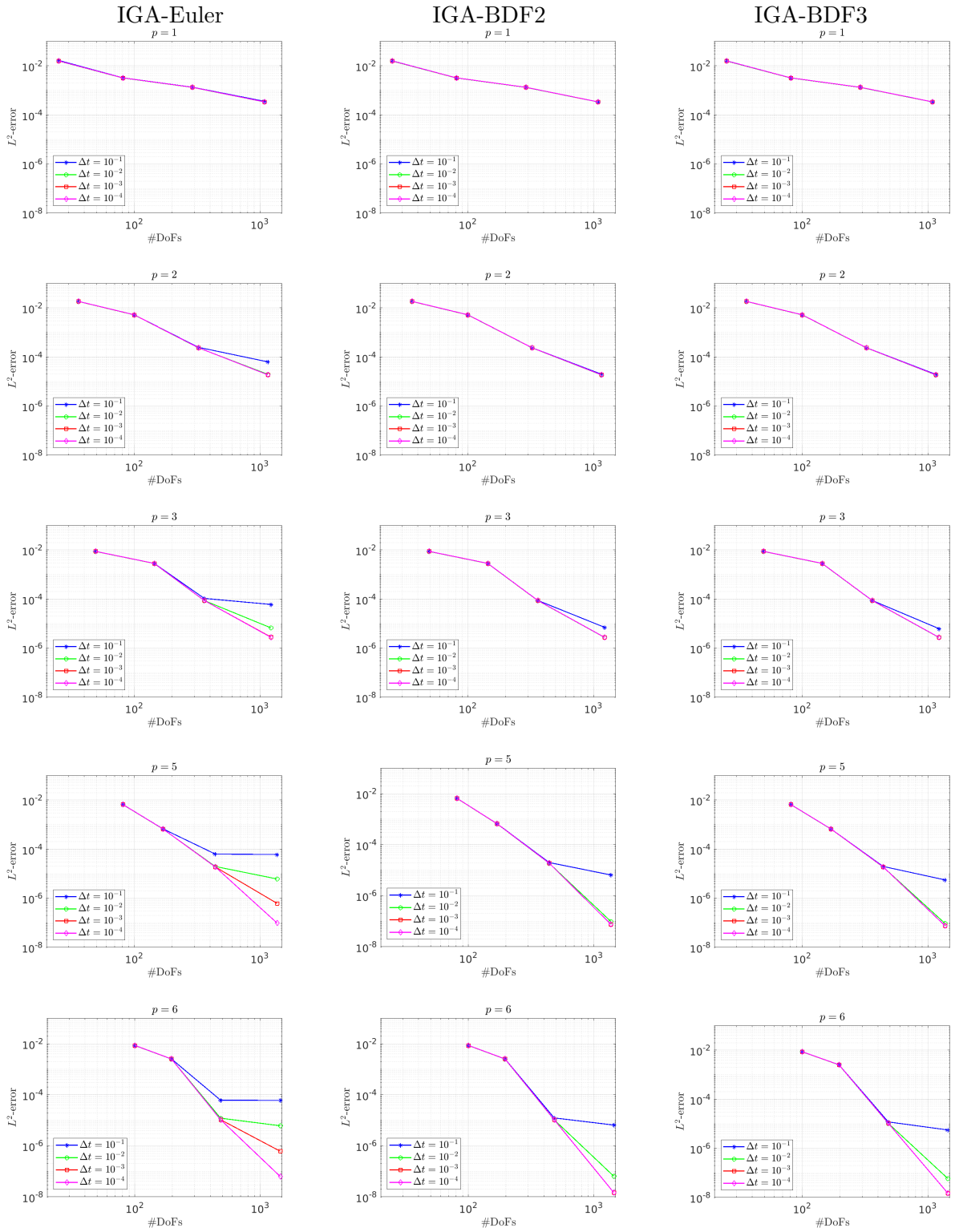

Figure 2: Convergence results at time $t = 1$ for the accuracy test using IGA-Euler (first column), IGA-BDF2 (second column) and IGA-BDF3 (third column) with $p = 1$ (first row) $p = 2$ (second row), $p = 3$ (third row), $p = 5$ (fourth row) and $p = 6$ (fifth row) using the considered timesteps $\Delta t = 10^{-1}$, 10^{-2}, 10^{-3} and 10^{-4}.

4.1 Accuracy test

In the first example, we aim to study the performance of different orders in space and time discretizations. Hence, we construct a numerical example with a predefined analytical solution so that the L^2-error in the numerical solution can be measured. The heat diffusion is defined by the following boundary-value problem

$$\begin{aligned} \frac{\partial u}{\partial t} - \lambda \nabla^2 u &= f, \qquad (t, \mathbf{x}) \in]0, T] \times \Omega, \\ u &= 0, \qquad (t, \mathbf{x}) \in]0, T] \times \Gamma, \\ u &= u_0, \qquad \text{at} \quad t = 0 \quad \text{and} \quad \mathbf{x} \in \Omega, \end{aligned} \tag{26}$$

where the problem domain is a squared plate $\Omega = [0, 2] \times [0, 2]$ exposed to the time-dependent heat source $f(t, \mathbf{x})$. The material properties are chosen to be $\alpha = 1$ and $\lambda = 0.1$. The boundary temperature is fixed and equals zero. The heat source as well as the initial domain temperatures are chosen so that the analytical solution is given as

$$u(x, y, t) = x^{20} y^{20} (2 - x)^{20} (2 - y)^{20} \left(1 - e^{-\lambda t}\right).$$

This the solution is challenging to recover as it involves steep gradients of a high polynomial order. It should also be mentioned that this is a benchmark problem first proposed in [27, 22]. The squared domain is discretized into uniform rectangular elements which are defined by the product of knot vectors. Starting from an initial mesh of 4×4 elements, four h-refinements (knots insertion) are considered where the number of elements is subsequently increased to 8×8, 16×16 and 32×32. All the considered refined meshes are also assumed to be uniform. Furthermore, each of the four meshes are then considered for a further p-refinement with p increased from $p = 1$ to 2, 3, 4, 5 and finally 6, hence, a total of 24 different spatial discretizations are used in this study. Each of these discretizations is then assessed for the three considered time integration schemes and for each of the following timesteps $\Delta t = 10^{-1}, 10^{-2}, 10^{-3}$ and 10^{-4}. Here, the error is evaluated at $t = 1$ using the L^2-norm. The error norm is integrated over the domain using a high-order Gauss quadrature. In order to eliminate any integration inaccuracy, the number of integration points is increased until the solution error converges in each mesh.

First, we evaluate the convergence with respect to the timestep Δt. Figure 2 shows the error convergence for different NURBS orders and for each of the three considered time integration schemes and the four timesteps. Using a high-order time integration scheme or a finer timestep does not change the error for $p = 1$. This is expected as at such a low IGA order the error is dominated by the inaccuracy in the spatial approximation. Hence, improving the time approximation by increasing the order or refining the timestep does not improve the error. Obviously, refining the mesh improves the error but even the highest refinement considered remains to be insensitive to the time approximation as $\Delta t = 10^{-1}$ is accurate enough in this case. These observations can also be made for the IGA with NURBS order $p = 2$. However, it is necessary to use a timestep smaller than $\Delta t = 10^{-1}$ to achieve an error improvement for the backward Euler integration scheme and only for the finest considered mesh. This refinement of timesteps is still unnecessary if a higher order time integration scheme is used. As can be seen in Figure 2, a timestep $\Delta t = 10^{-2}$ is enough to achieve the best possible error for all considered spatial resolutions in this case. Applying one further p-refinement, the previous behaviour becomes more pronounced and it is now possible to see the advantages of using a high-order time integration scheme. For $p = 3$, we can see error improvement by one order of magnitude when using the second-order or the third-order Adams-Bashforth method compared to the first-order backward Euler method for the timestep $\Delta t = 10^{-1}$. A similar advantage can also be observed for $\Delta t = 10^{-2}$ but for a smaller improvement in the error. At this level, a timestep $\Delta t = 10^{-3}$ or finer is needed to achieve the best possible error. One can see that the second-order and third-order Adams-Bashforth methods yield comparable results regardless of the timestep Δt. Applying further p-refinements, it becomes obvious the advantages of using higher order time integration methods and/or finer timesteps. Clearly, applying finer discretizations in space and/or in time decreases the error which is expected in this analysis. Figure 2 shows that, using the backward Euler method on the finest considered mesh, the error

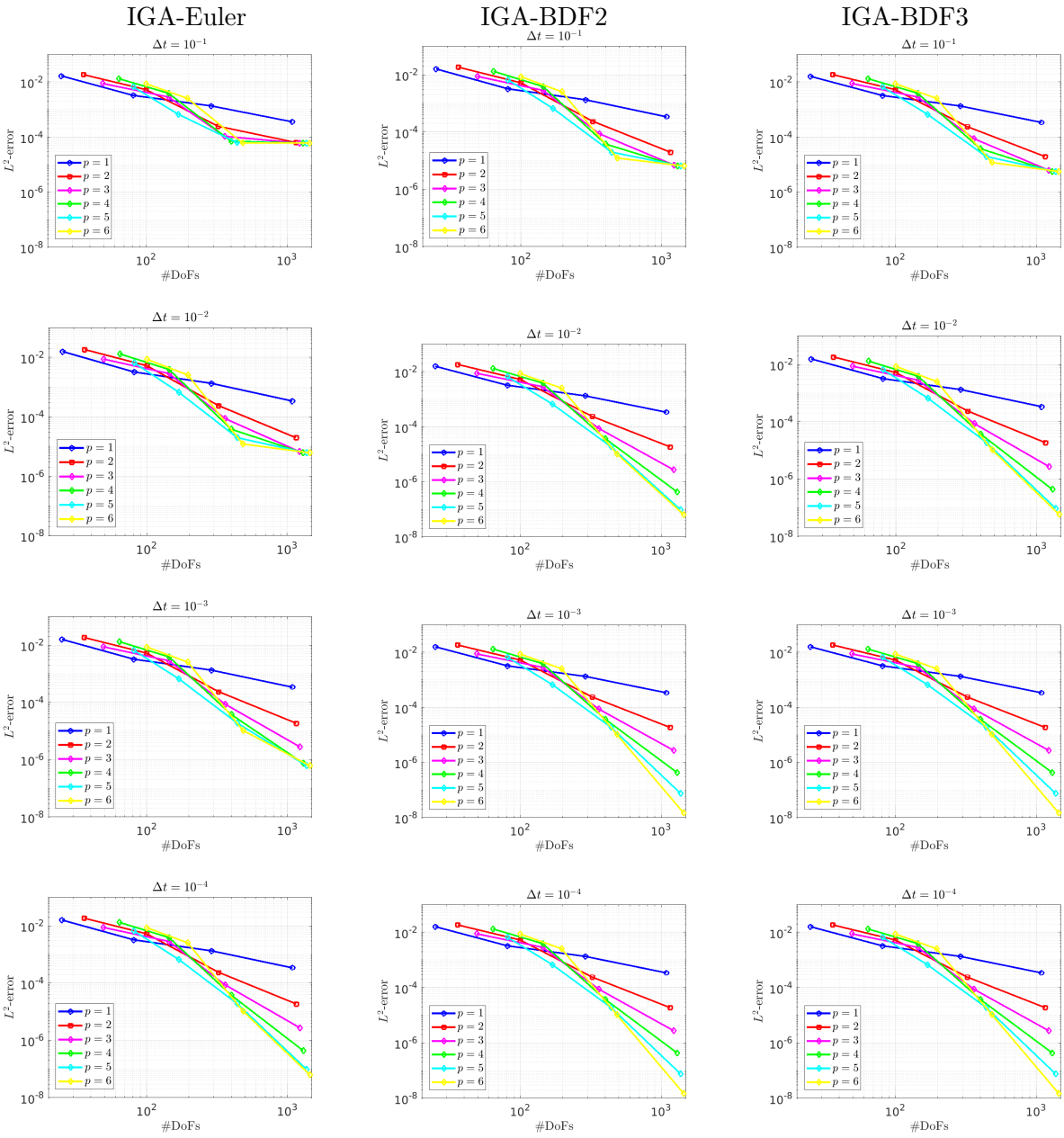

Figure 3: Convergence results at time $t = 1$ for the accuracy test using $\Delta t = 10^{-1}$ (first row) $\Delta t = 10^{-2}$ (second row), $\Delta t = 10^{-3}$ (third row) and $\Delta t = 10^{-4}$ (fourth row) for IGA-Euler (first column), IGA-BDF2 (second column) and IGA-BDF3 (third column) using the considered NURBS orders $p = 1, 2, 3, 4, 5$ and 6.

improves from around $8{\times}10^{-3}$ for all the considered timesteps with $p = 1$ to around $8{\times}10^{-8}$ for $\Delta t = 10^{-4}$ and $p = 5$. However, using this small timestep and again for $p = 5$, the error can be improved to 3×10^{-8} if the order of time integration is increased using the Adams-Bashforth methods where the second-order and the third-order schemes are relatively similar. The advantages of a higher order time integration scheme can be seen if a larger timestep is used. The error obtained using the Adams-Bashforth methods with a timestep $\Delta t = 10^{-2}$ is practically the same as the error obtained using the backward Euler method with $\Delta t = 10^{-4}$. This is a significant advantage as recovering the time history of the solution with $\Delta t = 10^{-2}$ requires 1% of the number of steps otherwise needed with $\Delta t = 10^{-4}$. Obviously, using the timestep $\Delta t = 10^{-2}$ with the backward Euler method leads to two orders of magnitude increase in the error. Applying one further p-refinement to $p = 6$, the improvement in the error becomes insignificant.

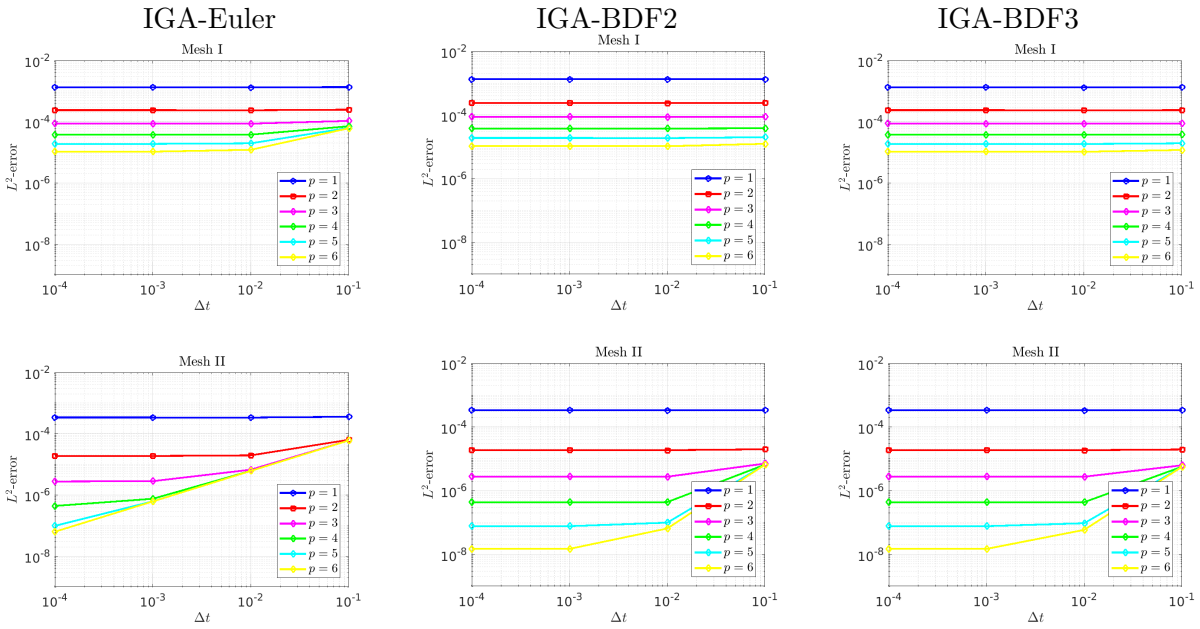

Figure 4: Convergence results at time $t = 1$ for the accuracy test using IGA-Euler (first column), IGA-BDF2 (second column) and IGA-BDF3 (third column) on the coarse mesh Mesh I (first row) and the fine mesh Mesh II (second row) using the considered NURBS orders $p = 1, 2, 3, 4, 5$ and 6.

Next, we rearrange the results so that we plot in Figure 3 the convergence errors with respect to the IGA order. It should be stressed that both figures 2 and 3 show the same results, however, in Figure 2 we plot the results so that the spatial convergence with respect to the polynomial order is studied while in Figure 3 the temporal convergence with respect to the timestep size is studied.

The results are grouped in Figure 3 according to the time integration scheme and the timestep. The figure shows that the convergence rates are significantly affected by the time integration errors. This is reflected in the large errors at coarse timesteps and lower order time integration. In these cases, increasing the IGA order to $p = 5$ or 6 is rather pointless as it leads to an increased computational cost but without any improvements in the solution accuracy. Refining the timestep and increasing the order of the time integration, one can see consequential improvements in the convergence rate of higher values of p. At $\Delta t = 10^{-3}$ and $\Delta t = 10^{-4}$ using the Adams-Bashforth methods, it is possible to attend the best convergence rates for the IGA with $p = 5$ and 6 which are not achieved otherwise. To better highlight this effect, we show in Figure 4 the error for individual NURBS order p plotted against the timestep. The plots are grouped according to the mesh and the time integration scheme. Clearly, refining the mesh leads to improved results until the point where the temporal error dominates the overall solution accuracy. This behaviour is observed mainly in higher order NURBS functions. To achieve the best possible error with $p = 6$, it is necessary to use the Adams-Bashforth methods with a maximum timestep $\Delta t = 10^{-3}$. Using the backward Euler and/or a larger timestep, leads to a temporal error dominance so that the advantages of using $p = 6$ are lost. The same behaviour is also observed but to a lower extent with other NURBS orders such as $p = 3, 4$ and 5.

To quantify the convergence rate we show in Table 1 the errors obtained with different time integration schemes and for $\Delta t = 10^{-1}$ and $\Delta t = 10^{-2}$ where the total number of degrees of freedom (DoFs) is also included. We also list below the errors the averaged convergence rate q for the IGA orders $p = 2, 4$ and 6. For $p = 2$ and to have a convergence rate higher than 2, it is necessary either to have a higher order time integration scheme or to refine the timestep to $\Delta t = 10^{-2}$. Both requirements are mandatory for $p = 4$ in order to reach a convergence rate higher than 4. For $p = 6$ using a high-order time integration scheme and $\Delta t = 10^{-2}$ still leads to a convergence rate of 5.4. Based on the observations made in this test, it is clear that using a high-order IGA to solve a problem is pointless unless accompanied with a higher order

Table 1: L^2-error at time $t = 1$ for the accuracy test using $\Delta t = 10^{-1}$ and $\Delta t = 10^{-2}$ in IGA-Euler, IGA-BDF2 and IGA-BDF3 on different meshes and the NURBS orders $p = 2, 4$ and 6.

$p = 2$

	$\Delta t = 10^{-1}$			$\Delta t = 10^{-2}$		
#DoFs	IGA-Euler	IGA-BDF2	IGA-BDF3	IGA-Euler	IGA-BDF2	IGA-BDF3
100	5.24E-03	5.24E-03	5.24E-03	5.19E-03	5.19E-03	5.19E-03
324	2.48E-04	2.39E-04	2.39E-04	2.37E-04	2.37E-04	2.37E-04
1156	6.34E-05	1.99E-05	1.96E-05	1.97E-05	1.86E-05	1.86E-05
	$q = 1.83$	$q = 2.29$	$q = 2.30$	$q = 2.29$	$q = 2.31$	$q = 2.31$

$p = 4$

	$\Delta t = 10^{-1}$			$\Delta t = 10^{-2}$		
#DoFs	IGA-Euler	IGA-BDF2	IGA-BDF3	IGA-Euler	IGA-BDF2	IGA-BDF3
144	3.90E-03	3.90E-03	3.90E-03	3.86E-03	3.86E-03	3.86E-03
400	7.11E-05	3.82E-05	3.81E-05	3.78E-05	3.73E-05	3.73E-05
1296	6.03E-05	6.53E-06	5.62E-06	6.13E-06	4.36E-07	4.35E-07
	$q = 2.03$	$q = 3.02$	$q = 3.08$	$q = 3.04$	$q = 4.16$	$q = 4.16$

$p = 6$

	$\Delta t = 10^{-1}$			$\Delta t = 10^{-2}$		
#DoFs	IGA-Euler	IGA-BDF2	IGA-BDF3	IGA-Euler	IGA-BDF2	IGA-BDF3
196	2.55E-03	2.55E-03	2.55E-03	2.52E-03	2.52E-03	2.52E-03
484	6.12E-05	1.24E-05	1.19E-05	1.21E-05	1.04E-05	1.04E-05
1444	6.03E-05	6.51E-06	5.61E-06	6.11E-06	6.48E-08	5.86E-08
	$q = 2.07$	$q = 3.24$	$q = 3.31$	$q = 3.27$	$q = 5.36$	$q = 5.41$

time integration scheme. This needs to be taken into consideration with higher order IGA as in this case the computational requirements increase significantly without any reward in the accuracy. In fact, it could even lead to large errors as is seen in some results in Figure 3.

To confirm the accuracy in modelling three-dimensional plates we solve the same problem but after extruding the domain into three dimensions *i.e.* $\mathbf{x} = (x, y, z)^\top$. A plate of 0.1 m thickness is considered so that the dimensions of the domain are now $2 \times 2 \times 0.1$ m. The heat source is retained as before but with a constant heat release across the thickness considering the relatively small thickness. The domain initial and ambient temperatures are kept unchanged. The same thermal conductivity and convective heat transfer coefficient are also unchanged. The NURBS basis are extend to three dimensions using the same tensorial product properties considered for the two dimensions case. The domain is meshed into 800 hexahedral elements of polynomial order $p = 5$, hence, a total Dofs= 4375. The considered uniform three-dimensional mesh is presented in figure 7. The time discretization is performed using the second order Adams-Bashford and $\Delta t = 0.1$. The obtained results are then compared to the two-dimensional case on a uniform mesh of 400 square elements with $p = 5$ and a total Dofs= 625 and using the same time discretization. Figure 7 shows the three-dimensional results at $t = 0.5, 5$ and 10 s. A quick comparison with results shown in Figure 6 at the same time instants we can see that the patterns obtained in two and three-dimensional cases are identical. Furthermore, in Figure 8 we show the evolution of the temperature at two points $A(1, 1, 0.05)$ and $B(1.5, 1, 0.05)$ in the three-dimensions results plotted against the two points $A(1, 1)$ and $B(1.5, 1)$ in

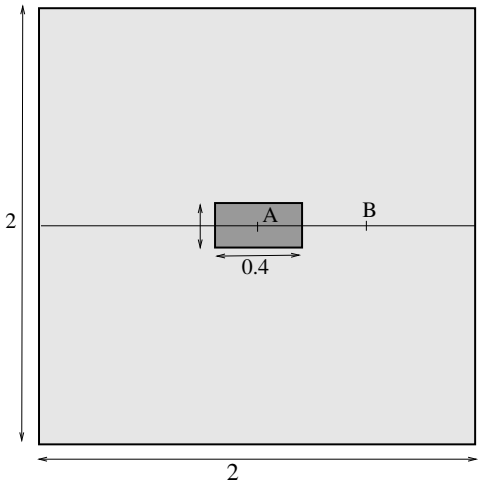

Figure 5: Heat transfer in a square plate configuration.

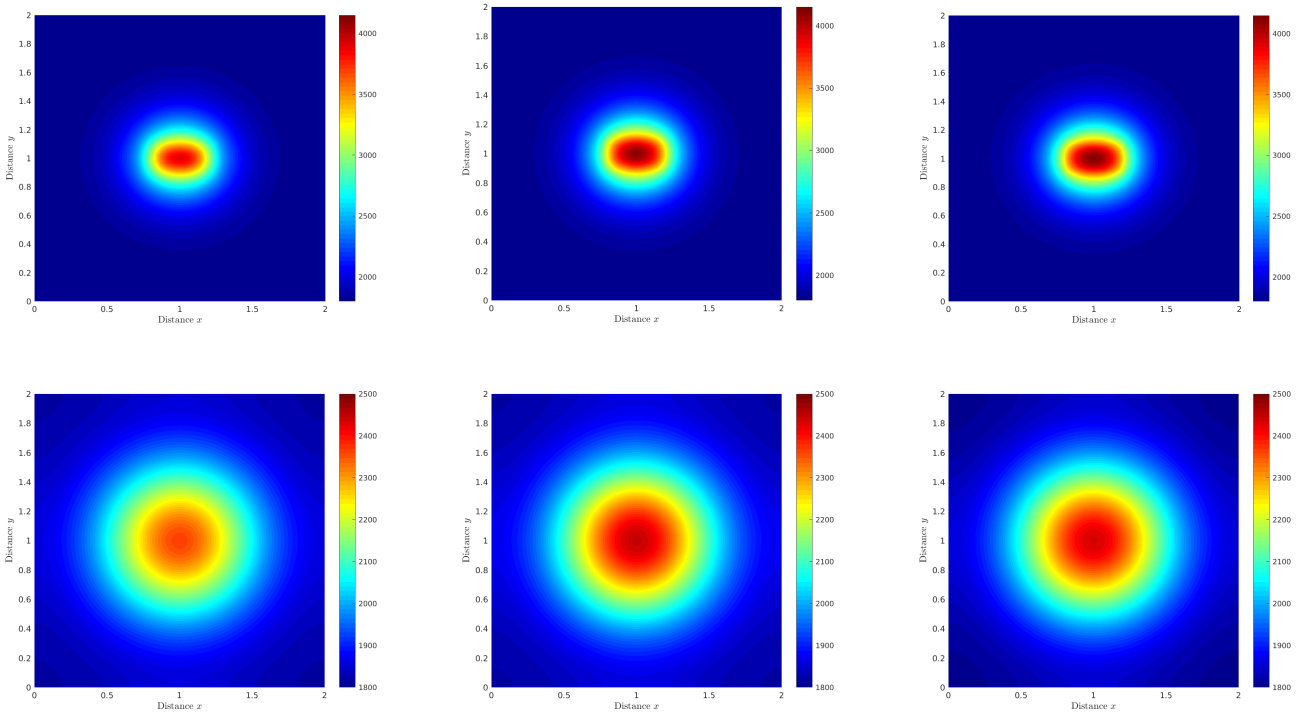

Figure 6: Snapshots of the temperature obtained for heat transfer in a square plate: (first row) at $t = 5\ s$ and (second row) at $t = 10\ s$ with IGA-BDF2 on the coarse mesh (first column), IGA-BDF2 on the fine mesh (second column) and the reference solution (third column).

two dimensions. The figure shows the results are well matched between the two- and three-dimensional cases.

4.2 Heat transfer in a square plate

In the second example, we consider a squared plate 2 m long with a heat source in the centre. The heat source is switched on for 5 seconds and we aim to understand the changes in the plate temperature within this time frame. We assume the domain is not heat-isolated *i.e.* it can exchange heat energy through its

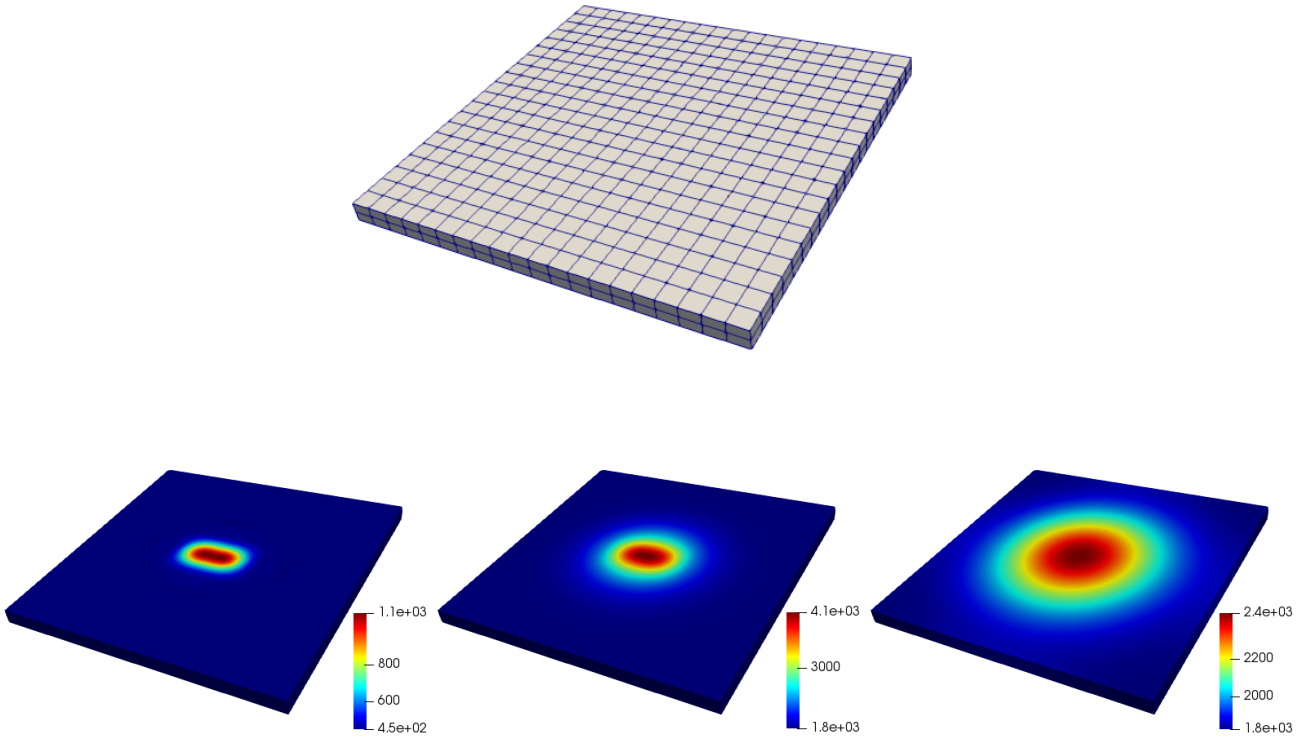

Figure 7: Single heat source in a three-dimensional plate. The top figure shows the considered IGA mesh with 800 elements and $Dofs = 4375$ while the bottom plots show the recovered heat transfer at the time instants $t = 0.5, 5$ and 10 s (left to right) and using BDF2 scheme with $\Delta t = 0.1$.

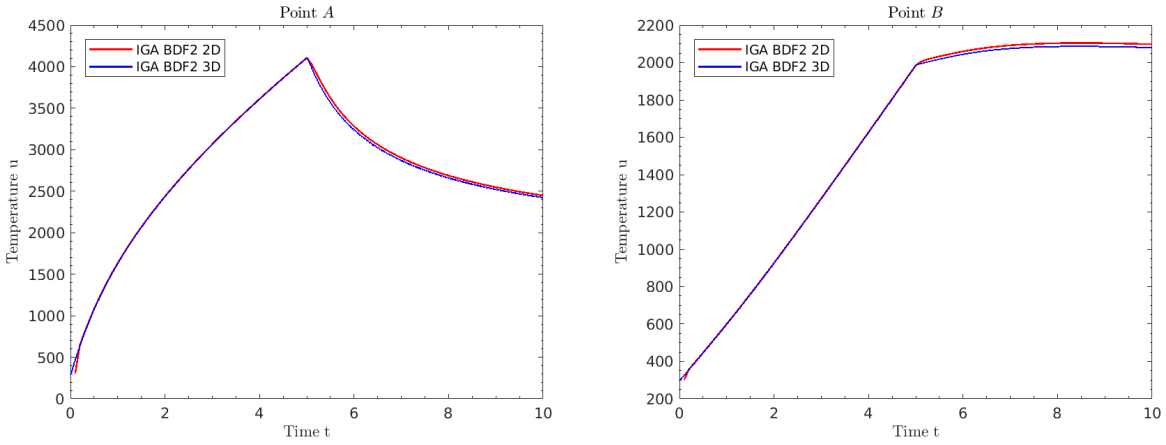

Figure 8: Time evolution for single heat source in two points: Heat transfer patterns compared at $A(1, 1, 0.05)$ and $B(1.5, 1, 0.05)$.

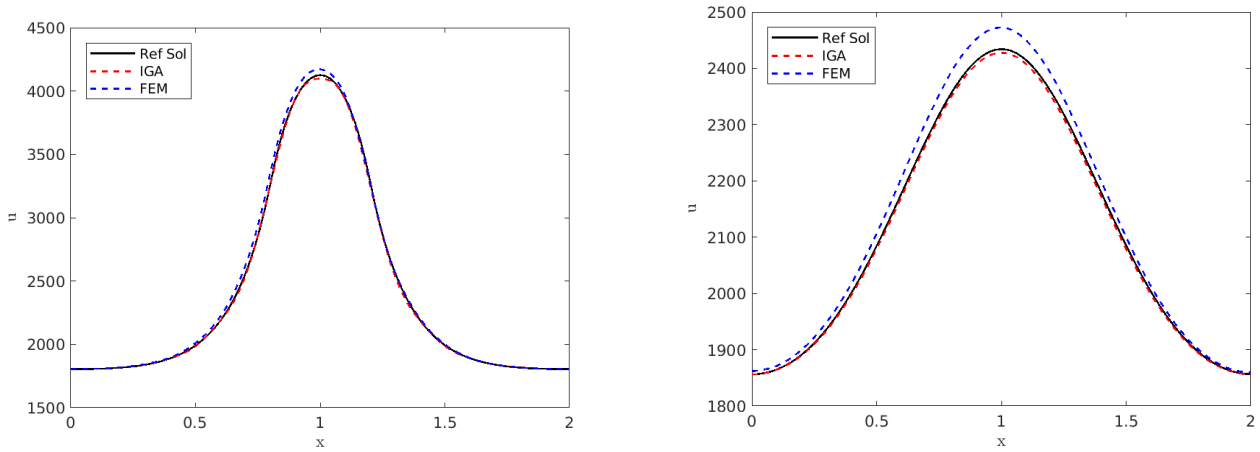

Figure 9: Cross-sections of the temperature at $y = 1$ obtained for the heat transfer in a square plate at time $t = 5\ s$ (left) and $t = 10\ s$ (right) using IGA-BDF2 method, FEM and the reference solution.

boundaries. The domain initial temperature is set to $u_0 = 300\ K$ which is also the ambient temperature $g(t, \mathbf{x}) = 300\ K$. The problem can be described using the following boundary-value problem

$$\begin{aligned} \frac{\partial u}{\partial t} - \lambda \nabla^2 u &= f, \qquad (t, \mathbf{x}) \in]0, T] \times \Omega, \\ \alpha u + \frac{\partial u}{\partial \mathbf{n}} &= g, \qquad (t, \mathbf{x}) \in]0, T] \times \Gamma, \\ u(0, \mathbf{x}) &= u_0, \qquad \text{at} \quad t = 0 \quad \text{and} \quad \mathbf{x} \in \Omega. \end{aligned} \tag{27}$$

The thermal conductivity of the medium is assumed to be $\lambda = 0.01\ kgm/Ks^2$ and the convective heat transfer coefficient $\alpha = 1\ \mathrm{kg/K}s^2$. The heat conductivity measures the material ability to conduct heat while the convective heat transfer coefficient measures the heat exchanged with the surrounding environment. The instantaneous source is given by

$$f = \begin{cases} 1800\ K/s, & \text{when} \quad \mathbf{x} \in [0.8, 0.9] \times [1.2, 1.1], \quad \text{and} \quad t \leq 5s, \\ \\ 300\ K/s, & \text{otherwise.} \end{cases}$$

A schematic plot of the problem and the heat source is found in Figure 5. As can be seen in the previous study, solving the problem using IGA-BFD2 method with NURBS order $p = 5$ can be an efficient combination to solve the problem using a minimum computational effort. The solution is first obtained on a relatively coarse mesh of 16×16 elements with $\Delta t = 0.1\ s$. Thus, the total DoFs is 441. To confirm the mesh convergence for this example, the problem is solved again on a finer mesh of 30×30 elements but with the same timesteps as before. The new mesh has 1225 total degrees of freedom. Finally, a reference solution is computed using the conventional FEM on a highly refined mesh and with a much smaller timestep $\Delta t = 0.001\ s$. Here, the reference solution is approximated using 125000 linear triangular elements resulting in 63001 degrees of freedom. The `FreeFEM++` software is used for the FEM solution [10]. Figure 6 shows the numerical solutions obtained at $t = 5$ and $10\ s$ using the IGA-BFD2 method for the considered timesteps and along with the reference solutions. These results show clearly IGA-BFD2 has converged to a similar solution to the one obtained using the FEM on a very refined mesh although in the former a much lower number of degrees of freedom is used. To compare the results further we also show in Figure 9 cross-sections of the three solutions at the same instants as in Figure 6. The numerical diffusion is very pronounced in the results obtained using the FEM whereas the results obtained using the IGA-BFD2 method and the

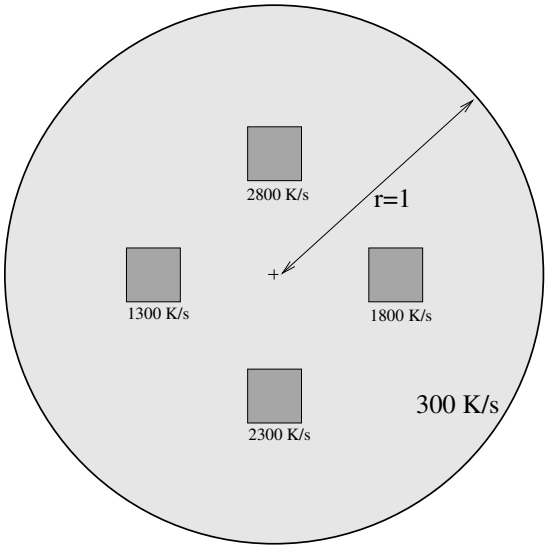

Figure 10: Heat transfer in a circular plate configuration.

reference solutions exhibit the same behaviour with very little numerical diffusion. This numerical diffusion in the FEM results becomes larger at time $t = 10\ s$ than at earlier time $t = 5\ s$ which is mainly due to the error accumulations during the time integration. The plots also confirm the previous conclusions about the efficiency of the IGA at higher orders for this class of heat conduction problems. The proposed IGA-BFD2 method as can be seen in the results performs well. The solution in this case is accurate and stable even on coarse meshes and/or coarse timesteps. It should be mentioned that the efficiency of the proposed approach is reflected in the reduction in the total number of degrees of freedom and the reduction in the number of timesteps. The code developed in this work needed significantly less CPU time when solving the problem compared to `FreeFEM`$^{++}$. However, we avoided CPU time comparisons as our code and `FreeFEM`$^{++}$ are implemented differently. Hence, the CPU time reduction in our code is the result of improved efficiency in the method as well as the optimized implementation of our code. Therefore, we restrict our comparisons to the number of degrees of freedom and the number of timesteps.

4.3 Heat transfer in a circular plate

The last example shows a benchmark case study of heat transfer in a circular plate proposed in [27]. The problem domain is circular with multiple heat sources of different magnitudes. The heat sources are switched on at $t = 0$ and then off at $t = 5\ s$ and the problem is modelled for the time domain of 10 s. The boundary value problem of this problem is defined by (27). The domain is a unit circle centered at $(0, 0)^\top$. A schematic plot of the problem domain is included in Figure 10. The domain initial temperature is $u_0 = 300\ K$. The ambient temperature is also assumed to be $g = 300\ K$. The thermal conductivity is given by $\lambda = 0.01\ kgm/Ks^2$ while the convective heat transfer coefficient $\alpha = 1\ kg/Ks^2$. The heat sources are supposed to be rectangular and located at different parts of the computational domain. Notice that the IGA employs directly the geometry provided by the CAD in terms of NURBS and it approximates the finite element solutions using these NURBS as basis functions. Therefore, some common complex geometries, such as circular plates, are exactly described. In contrast to the conventional FEM, irregular geometries are precisely incorporated at the coarsest mesh level in the IGA. The sources location and intensities are give by

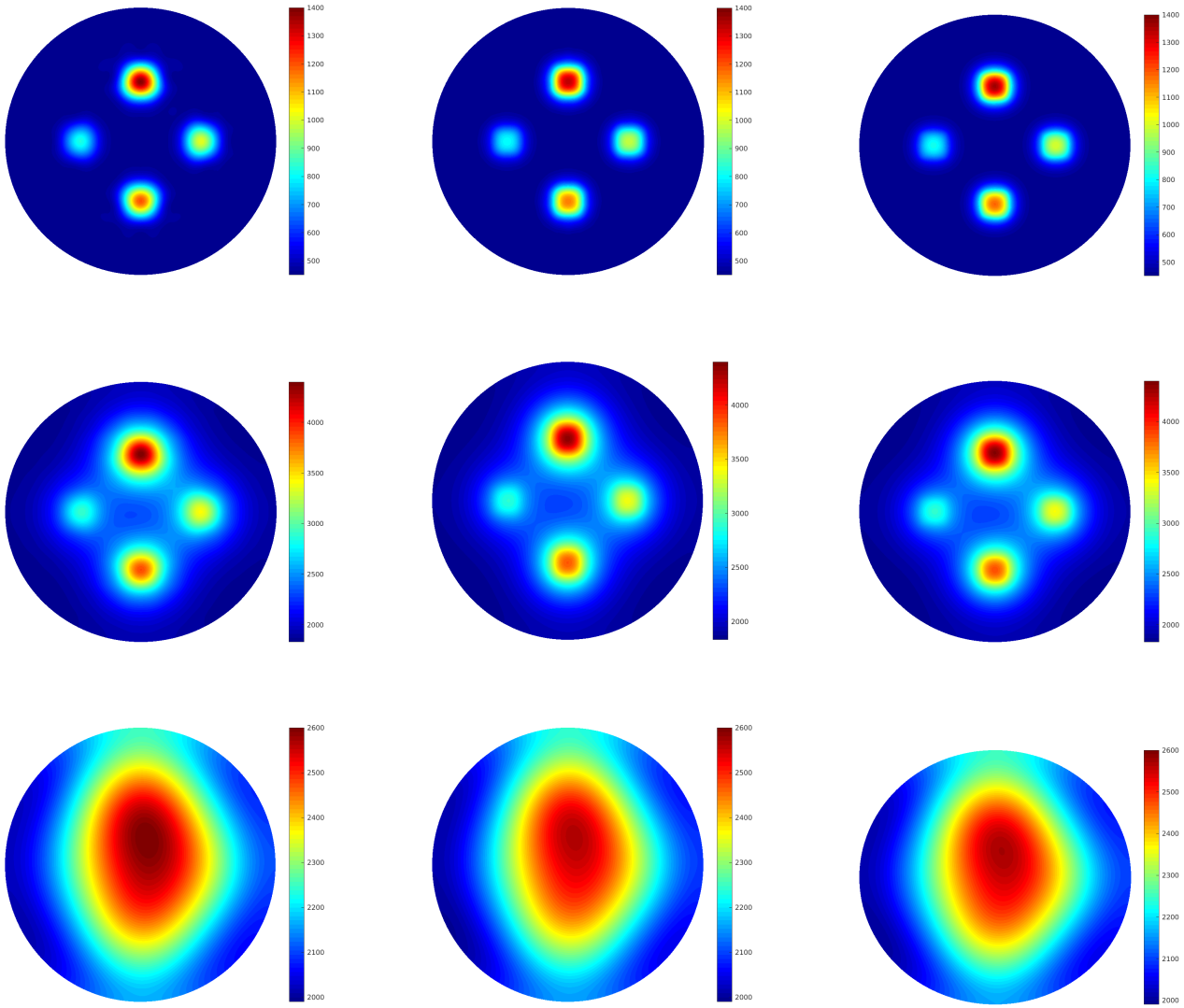

Figure 11: Snapshots of the temperature obtained for the heat transfer in a circular plate at time $t = 0.5\ s$ (first row) and $t = 5\ s$ (second row) and $t = 10\ s$ (third row) using IGA-BDF2 method on the coarse mesh (first column), IGA-BDF2 method on the fine mesh (second column) and the reference solution (third column).

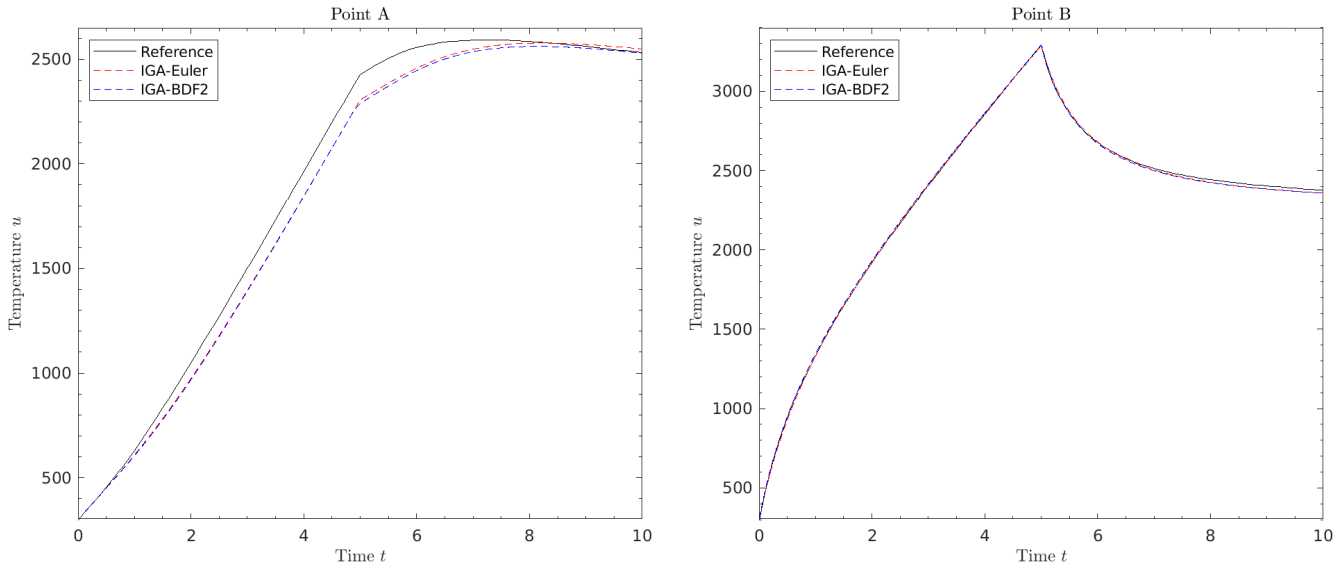

Figure 12: The temperature change in time at the points A (left) and B (right) obtained for the heat transfer in a circular plate using a mesh with 40×40 elements.

Table 2: Computational costs in seconds, minimum and maximum values of the temperature in K for the heat transfer in a circular plate at $t = 0.5\ s$ using $\Delta t = 0.01\ s$ on two different meshes.

	Coarse mesh			Fine mesh		
	$\max u$	$\min u$	CPU	$\max u$	$\min u$	CPU
IGA-Euler	1367.9	449.8825	58.20	1362.4	449.9663	86.09
IGA-BDF2	1372.0	449.8712	59.11	1366.5	449.9617	86.64
IGA-BDF3	1371.9	449.8707	59.17	1366.4	449.9615	86.95
Reference	1360	450	1226.8	1360	450	1226.8

$$f = \begin{cases} 1300\ K/s, & \text{when} \quad \mathbf{x} \in [-0.55, -0.35] \times [-0.1, 0.1], \quad \text{and} \quad t \leq 5\ s, \\ 1800\ K/s, & \text{when} \quad \mathbf{x} \in [0.35, 0.55] \times [-0.1, 0.1], \quad \text{and} \quad t \leq 5\ s, \\ 2300\ K/s, & \text{when} \quad \mathbf{x} \in [-0.1, 0.1] \times [-0.55, -0.35], \quad \text{and} \quad t \leq 5\ s, \\ 2800\ K/s, & \text{when} \quad \mathbf{x} \in [-0.1, 0.1] \times [0.35, 0.55], \quad \text{and} \quad t \leq 5\ s, \\ 300\ K/s, & \text{otherwise.} \end{cases}$$

The problem is solved using IGA with $p = 5$ and the second-order Adams-Bashforth method. The IGA solution is based on a coarse mesh grid of 16×16 elements (DoFs = 441) and a fine one of 32×32 elements (DoFs = 1369). To obtain a reference solution for this example a highly refined FEM mesh is used. Only linear triangular elements are considered in the FEM with a total number of 14060 nodes. The numerical results at $t = 0.5$, 5 and 10 s using a fixed timestep $\Delta t = 0.01$ are plotted and compared in Figure 11 to the reference solution at the same time instants. It can be seen from the figure that both methods have produced very similar results despite the much higher number of DoFs needed with the FEM. Next, we present in Figure 12 the change in the temperatures over time at two points A and B located at $(0, 0)^\top$

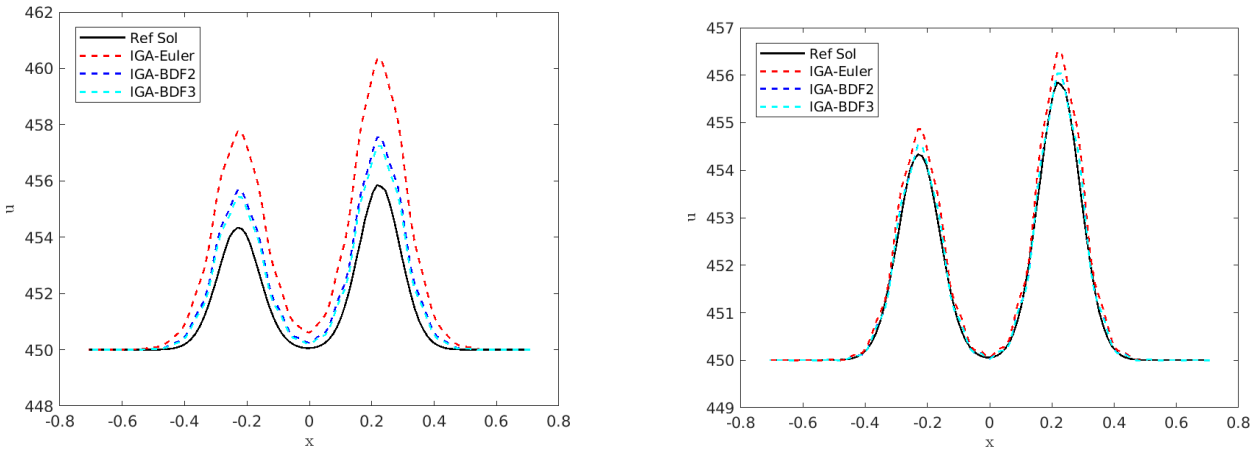

Figure 13: The temperature cross-sections at the line passing through the points $(-0.5, -0.5)$ and $(0.5, 0.5)$ obtained for the heat transfer in a circular plate at time $t = 0.5\ s$ using $\Delta t = 0.01\ s$ (left) and $\Delta t = 0.001\ s$ (right) using a mesh with 40×40 elements.

and $(0.5, 0)^\top$, respectively. Here, we present results obtained using the first-order backward Euler method, the second-order Adams-Bashforth method and the reference solutions. It is evident that no noticeable differences have been detected in the results obtained at the point B whereas at the point A, differences between the IGA and reference solutions are seen in the these results particularly at time $t = 5\ s$ when the heat source is switched off. It should be noted that using only few elements in the IGA for this example, it is possible to have an exact representation for the circular geometry. However, using Lagrangian-based finite elements it is not possible to have exact representation for a circular geometry. The ability to model exact geometries on coarse mesh grids is in fact a major advantage for the IGA compared to the conventional FEM.

To examine the effect of timestep on the results, we display in Figure 13 the temperature cross-sections at the line passing through the points $(-0.5, -0.5)$ and $(0.5, 0.5)$ obtained times $t = 0.5\ s$ on the coarse mesh using $\Delta t = 0.01\ s$ and $\Delta t = 0.001\ s$. It is evident that, the larger the timestep Δt is, the higher the numerical diffusion of the computed results. Compared to the reference solution, the second-order and third-order Adams-Bashforth methods yield similar accuracy and more accurate than its first-order counterpart. Reducing the timestep from $\Delta t = 0.01\ s$ to $\Delta t = 0.001\ s$ results in an increase in the accuracy for all considered time stepping schemes but the first-order backward Euler method is the least accurate. To further quantify the results for this example, we summarize in Table 2 the maximum and minimum temperatures in the computational domain along with the computational costs obtained for the considered time stepping schemes and the reference solutions on the coarse and fine meshes at time $t = 0.5\ s$ using $\Delta t = 0.01\ s$. The results obtained using the second-order and third-order Adams-Bashforth methods are similar to those obtained for the reference solution which confirm their better accuracy compared to the first-order backward Euler method. A simple inspection of the CPU times in Table 2 reveals that the three considered time stepping schemes exhibit roughly the same computational cost but the reference results obtained using the FEM require a much larger amount of CPU times. Finally, we also note that the proposed combination of high-order isogeometric analysis with high-order time integration schemes is highly attractive. The computed solutions remain stable and accurate even on coarse mesh grids and large timesteps.

5 Conclusion

We investigate transient heat transfer in plates within the context of fire-structure interaction. To recover the heat transfer in space and in time, we proposed using high-order isogeometric analysis (IGA) and high-order time integration schemes. The proposed approach has several advantages compared to standard methods. First, the high-order inter-element continuity with IGA eliminates the need to rotational degrees of freedom when modelling the stresses within a plate. For a given problem this significantly reduces the required total number of degrees of freedom compared to the two-dimensional finite elements. Moreover, using three-dimensional finite elements to model the plate although remove the need for rotational degrees of freedom but it can result into a major increase in the total number of degrees of freedom. The increase is necessary to achieve moderate elements aspect ratio as the plate thickness is much smaller than the other dimensions. Based on this, the exact same mesh can be used for heat transfer as well as for stress analysis which simplify their coupling so that the exchange of information between the heat transfer and the stress analysis is significantly easier compared to using two different meshes. Furthermore, the isogeometric analysis enables exact representation of any complex geometries without the need to refine the mesh which could be specially useful for those problems sensitive to accurate geometries. Finally, using higher order isogeometric analysis it is possible to achieve high accuracy with fewer degrees of freedom which improves the efficiency. The use of high-order time integration schemes would help to achieve the full potential of high-order isogeometric analysis. The proposed approach is evaluated using three test cases. The exact solution is predefined in the first test example which helps to measure the error of the proposed approach. For the last two examples, finite element solutions are created using highly refined meshes. The accuracy, the efficiency and the stability of the proposed approach are confirmed in the presented results. The proposed approach can also be useful for analyzing heat transfer in three-dimensional shells. However, in this case it is not always possible to represent the fire as in-plane heat source. This will be studied in a future work.

References

[1] Z. An, T. Yu, T.Q. Bui, C. Wang, and N.A. Trinh. Implementation of isogeometric boundary element method for 2-D steady heat transfer analysis. *Advances in Engineering Software*, 116:36–49, 2018.

[2] D. Anders, K. Weinberg, and R. Reichardt. Isogeometric analysis of thermal diffusion in binary blends. *Computational Materials Science*, 52(1):182–188, 2012.

[3] P. Benedusi, P. Ferrari, C. Garoni, R. Krause, and S. Serra-Capizzano. Fast Parallel Solver for the Space-time IgA-DG Discretization of the Diffusion Equation. *Journal of Scientific Computing*, 89(1):1–21, 2021.

[4] J.C. Butcher and G. Wanner. Runge-Kutta methods: some historical notes. *Applied Numerical Mathematics*, 22(1-3):113–151, 1996.

[5] C. De Falco, A. Reali, and R. Vázquez. GeoPDEs: A research tool for Isogeometric Analysis of PDEs. *Advances in Engineering Software*, 42(12):1020–1034, 2011.

[6] R. Deokar, D. Maxam, and K. K. Tamma. A novel and simple a posteriori error estimator for LMS methods under the umbrella of GSSSS framework: Adaptive time stepping in second-order dynamical systems. *Computer Methods in Applied Mechanics and Engineering*, 334:414–439, 2018.

[7] I.S. Duff and J.K. Reid. The multifrontal solution of indefinite sparse symmetric linear. *ACM Transactions on Mathematical Software (TOMS)*, 9(3):302–325, 1983.

[8] P. Gervasio, L. Dedè, O. Chanon, and A. Quarteroni. A Computational Comparison Between Isogeometric Analysis and Spectral Element Methods: Accuracy and Spectral Properties. *Journal of Scientific Computing*, 83(1), 2020.

[9] Q. Guo and A.E. Jeffers. Direct differentiation method for response sensitivity analysis of structures in fire. *Engineering Structures*, 77:172–180, 2014.

[10] F. Hecht. New development in freefem++. *Journal of Numerical Mathematics*, 20(3-4):251–265, 2012.

[11] T. J.R. Hughes, J. A. Cottrell, and Y. Bazilevs. Isogeometric analysis: CAD, finite elements, NURBS, exact geometry and mesh refinement. *Computer Methods in Applied Mechanics and Engineering*, 194(39-41):4135–4195, 2005.

[12] Chennakesava Kadapa and Mokarram Hossain. A robust and computationally efficient finite element framework for coupled electromechanics. *Computer Methods in Applied Mechanics and Engineering*, 372:113443, 2020.

[13] Chennakesava Kadapa, Zhanfeng Li, Mokarram Hossain, and Jiong Wang. On the advantages of mixed formulation and higher-order elements for computational morphoelasticity. *Journal of the Mechanics and Physics of Solids*, 148:104289, 2021.

[14] K.J. Bathe. *Finite Element Procedures*. Klaus-Jurgen Bathe, 2005.

[15] Y. Lai, Y.J. Zhang, L. Liu, X. Wei, E. Fang, and J. Lua. Integrating CAD with Abaqus: A practical isogeometric analysis software platform for industrial applications. *Computers and Mathematics with Applications*, 74(7):1648–1660, 2017.

[16] N. Liu, P.A. Beata, and A.E. Jeffers. A mixed isogeometric analysis and control volume approach for heat transfer analysis of nonuniformly heated plates. *Numerical Heat Transfer, Part B: Fundamentals*, 75(6):347–362, 2019.

[17] N. Liu and A.E. Jeffers. A geometrically exact isogeometric Kirchhoff plate: Feature-preserving automatic meshing and C1 rational triangular Bézier spline discretizations. *International Journal for Numerical Methods in Engineering*, 115(3):395–409, 2018.

[18] C. Manni, F. Pelosi, and M.L. Sampoli. Isogeometric analysis in advection-diffusion problems: Tension splines approximation. *Journal of Computational and Applied Mathematics*, 236(4):511–528, 2011.

[19] S. U. Masuri, M. Sellier, X. Zhou, and K. K. Tamma. Design of order-preserving algorithms for transient first-order systems with controllable numerical dissipation. *International Journal for Numerical Methods in Engineering*, 88(13):1411–1448, 2011.

[20] D. Maxam, R. Deokar, and K. K. Tamma. A unified computational methodology for dynamic thermoelasticity with multiple subdomains under the GSSSS framework involving differential algebraic equation systems. *Journal of Thermal Stresses*, 42(1):163–184, 2019.

[21] K. McGrattan, S. Hostikka, R. McDermott, J. Floyd, C. Weinschenk, and K. Overholt. Fire Dynamics Simulator, User's Guide, Sixth Edition, 2013.

[22] M Shadi Mohamed, Mohammed Seaid, Jon Trevelyan, and Omar Laghrouche. Time-independent hybrid enrichment for finite element solution of transient conduction–radiation in diffusive grey media. *Journal of Computational Physics*, 251:81–101, 2013.

[23] V.P. Nguyen, C. Anitescu, S.P.A. Bordas, and T. Rabczuk. Isogeometric analysis: An overview and computer implementation aspects. *Mathematics and Computers in Simulation*, 117:89–116, 2015.

[24] Alessandro Nitti, Josef Kiendl, Alessio Gizzi, Alessandro Reali, and Marco D. de Tullio. A curvilinear isogeometric framework for the electromechanical activation of thin muscular tissues. *Computer Methods in Applied Mechanics and Engineering*, 382:113877, 2021.

[25] Les Piegl and Wayne Tiller. *Nurbs Book*. 1997.

[26] A. Quarteroni, R. Sacco, and F. Saleri. *Méthodes Numériques: Algorithmes, analyse et applications*. Springer Science & Business Media, 2007.

[27] M. Shadi Mohamed, Mohammed Seaid, Jon Trevelyan, and Omar Laghrouche. A partition of unity FEM for time-dependent diffusion problems using multiple enrichment functions. *International Journal for Numerical Methods in Engineering*, 93(3):245–265, 2013.

[28] N Thiyaneshwaran, K Sivaprasad, and B Ravisankar. Characterization based analysis on tial3 intermetallic phase layer growth phenomenon and kinetics in diffusion bonded ti/tial3/al laminates. *Materials Characterization*, 174:110981, 2021.

[29] V.N. Van Do and C.H. Lee. Isogeometric layerwise formulation for bending and free vibration analysis of laminated composite plates. *Acta Mechanica*, 232(4):1329–1351, 2021.

[30] R. Vázquez. A new design for the implementation of isogeometric analysis in Octave and Matlab: GeoPDEs 3.0. *Computers and Mathematics with Applications*, 72(3):523–554, 2016.

[31] A. V. Vuong, Ch. Heinrich, and B. Simeon. ISOGAT: A 2D tutorial MATLAB code for Isogeometric Analysis. *Computer Aided Geometric Design*, 27(8):644–655, 2010.

[32] Y. Wang, K. Tamma, D. Maxam, T. Xue, and G. Qin. An Overview of High-Order Implicit Algorithms for First-/Second-Order Systems and Novel Explicit Algorithm Designs for First-Order System Representations. *Archives of Computational Methods in Engineering*, 28(5):3593–3619, 2021.

[33] R. Willems, L.A.J. Friedrich, and C.V. Verhoosel. Finite Element Analysis of Laminar Heat Transfer within an Axial-Flux Permanent Magnet Machine. *Mathematical and Computational Applications*, 26(1):23, 2021.

[34] T. Xue and X. Zhang. Generalized heat conduction model involving imperfect thermal contact surface: Application of the GSSSS-1 differential-algebraic equation time integration. *International Journal of Heat and Mass Transfer*, 116:889–896, 2018.

[35] T. Yu, B. Chen, S. Natarajan, and T.Q. Bui. A locally refined adaptive isogeometric analysis for steady-state heat conduction problems. *Engineering Analysis with Boundary Elements*, 117:119–131, 2020.

[36] O.C. Zienkiewicz. Introductory Lectures on the Finite Element Method. *Introductory Lectures on the Finite Element Method*, 1972.